Optical signatures of type-II Weyl fermions in the noncentrosymmetric semimetals RAlSi (R=La, Ce, Pr, Nd, Sm)

J. Kunze, M. Köpf, Weizheng Cao, Yanpeng Qi, Christine A. Kuntscher

Optical signatures of type-II Weyl fermions in the noncentrosymmetric semimetals RAlSi (R = La, Ce, Pr, Nd, Sm)

J. Kunze,[1] M. Köpf,[1] Weizheng Cao,[2,*] Yanpeng Qi,[2,3,4,†] and C. A. Kuntscher[1,‡]

[1]*Experimental Physics II, Institute of Physics, University of Augsburg, 86159 Augsburg, Germany*

[2]*School of Physical Science and Technology, ShanghaiTech University, Shanghai 201210, China*

[3]*ShanghaiTech Laboratory for Topological Physics, ShanghaiTech University, Shanghai 201210, China*

[4]*Shanghai Key Laboratory of High-resolution Electron Microscopy and ShanghaiTech Laboratory for Topological Physics, ShanghaiTech University, Shanghai 201210, China*

Weyl semimetals with magnetic ordering provide a promising platform for the investigation of rare topological effects such as the anomalous Hall effect, resulting from the interplay of nontrivial bands with various spin configurations. The materials RAlSi, where R represents a rare-earth element, are prominent representatives of Weyl semimetals, where the Weyl states are induced by space inversion symmetry breaking, and in addition, for several rare-earth elements R, enhanced by time-reversal symmetry breaking through the formation of a magnetic order at low temperature. We report optical signatures of Weyl fermions in the magnetic compounds CeAlSi, PrAlSi, NdAlSi, and SmAlSi as well as the nonmagnetic family member LaAlSi by broad-frequency infrared spectroscopy at room temperature, i.e., in the paramagnetic phase. A similar profile of the optical conductivity spectrum and a metallic character are observed for all compounds, with LaAlSi showing the strongest free charge-carrier contribution. Furthermore, the linear-in-frequency behavior of the optical conductivity of all investigated compounds indicates the presence of Weyl nodes in close proximity to the Fermi energy, resulting from inversion symmetry breaking in noncentrosymmetric structures. According to the characteristics of these linear slopes, the RAlSi compounds are expected to host mainly type-II Weyl states with overtilted Weyl cones. The results are compared to the optical response of the closely related RAlGe materials, which are considered as potential hybridization-driven Weyl-Kondo systems.

I. INTRODUCTION

In recent years, the investigation of topological phases in condensed matter has attracted a lot of interest. A prominent example is the Dirac semimetal phase, where linear band crossings occur near the Fermi energy E_F, and they are protected by spatial and/or time-reversal symmetry [1]. Other than high-symmetric Dirac points, the existence of Weyl points requires either inversion or time-reversal symmetry to be broken, creating pairs of Weyl points with different chirality [2]. One famous representative of such Weyl semimetals (WSMs) with broken inversion symmetry is the noncentrosymmetric and nonmagnetic compound TaAs [3]. When the degeneracy of the Dirac cones is lifted by the broken inversion symmetry, the Weyl cones are shifted in energy relative to each other, whereas breaking of time-reversal symmetry through magnetic moments causes a shift in k-space [4,5]. WSMs with broken time-reversal symmetry are rare as compared to those with broken inversion symmetry, yet promising since in inversion symmetric systems there is no shift of the nodes in energy, resulting in a vanishing density of states

at the Fermi level [4]. In addition, the combination of topological phases and magnetism enables the realization of rare quantum-mechanical effects, such as the intrinsic anomalous Hall effect or the topological Hall effect [6,7]. EuCd$_2$As$_2$ represents this group as a famous member, where the alignment of Eu spins magnetically induces Weyl nodes via exchange coupling to create a magnetic WSM candidate [4].

The family of rare-earth-based compounds RAlX (R = La, Ce, Pr, Nd, Sm; X = Si and Ge) also has attracted a lot of attention recently as WSM candidates [8–13]. The noncentrosymmetric RAlX family allows the investigation of WSM states in magnetic and nonmagnetic phases in isostructural compounds, as the magnetic contributions depend on the rare-earth element R [11]. Among the La, Ce, Pr, Nd, and Sm elements, only La does not exhibit a magnetic moment in the RAlSi compounds [14]. Therefore, varying the rare-earth ion affects the electronic topology through different magnetic ground states [15]. In the case of PrAlSi, a ferromagnetic order sets in at T_C = 17.8 K, followed by two spin-glass-like reentrant magnetic transitions at lower temperatures [8]. There are also several critical temperatures for NdAlSi, as this compound undergoes an antiferromagnetic transition at T_N = 7.2 K and a ferrimagnetic transition at T_C = 3.3 K [7,16]. SmAlSi orders antiferromagnetically at T_N = 10.7 K, while CeAlSi also shows a ferromagnetic magnetic structure below T_C = 9.4 K [15]. RAlSi compounds crystallize for the most

*caowzh@shanghaitech.edu.cn

†qiyp@shanghaitech.edu.cn

‡christine.kuntscher@physik.uni-augsburg.de

part in the space group $I4_1md$, yet with a certain percentage also the $I4_1/amd$ phase has been found experimentally [14]. In the main space group $I4_1md$, the unit-cell parameters of RAlSi vary between $a = 4.1566$ Å for Sm and $a = 4.3069$ Å for La, and $c = 14.4552$ Å for Sm and $c = 14.6494$ Å for La [14].

Regarding the electronic structure, the RAlX compounds have been shown to be promising candidates for the WSM phase, as numerous Weyl points are reported to exist near the Fermi level, e.g., 40 Weyl points in the paramagnetic phase of NdAlSi [7], CeAlSi [17], and LaAlGe [12] upon inclusion of spin-orbit coupling. The electronic band structure of RAlSi is very similar among the different compounds, and the density of states at the Fermi level is expected to be vanishingly small, which leads to a semimetallic ground state [6,11,16,18]. Resistivity measurements have confirmed the (semi)metallic behavior of the RAlSi materials as dc conductivity values between 11 000 and 18 000 Ω^{-1} cm^{-1} have been found in recent publications [7,8,15].

The materials CeAlGe and PrAlGe are furthermore discussed as potential hybridization-driven Weyl-Kondo semimetals [19,20]. According to optical conductivity studies, electronic correlations due to the hybridization of the localized f electrons of the rare-earth element (Ce $4f^1$ and Pr $4f^2$) with the conduction electron states lead to a reduction of the Fermi velocity and an enhancement of the charge-carrier effective mass, in contrast to LaAlGe lacking f electrons (La $4f^0$). It was furthermore reported that the onset of magnetic ordering in CeAlGe and PrAlGe significantly affects the electronic band structure, as observed in the temperature-dependent optical response [19,20], suggesting a coupling between magnetism and the electronic degrees of freedom. In contrast, recent angle-resolved photoemission spectroscopy results combined with first-principles calculations for PrAlSi and SmAlSi revealed only a weak coupling between the localized $4f$ electrons and the conduction electrons and a negligible effect of the magnetic ordering on the electronic band structure [18]. Accordingly, whether the RAlX are indeed Weyl-Kondo systems is still a matter of debate.

In this work, the optical response of RAlSi ($R = $ La, Ce, Pr, Nd, Sm) is investigated by comparing the optical functions such as the optical conductivity and the dielectric function of the various rare-earth-based compounds. The results are discussed in terms of the transport and topological properties discussed in the literature [5,7,8,15]. In particular, a comparison to the optical conductivity of the closely related RAlGe materials is given.

II. METHODS

Single crystals of RAlSi were synthesized using the self-flux method, as described elsewhere [15,21]. The dimensions of these platelike samples are in the range of 0.5–3 mm, and high-quality surfaces have been prepared by careful polishing, as they are essential for quantitative infrared reflectivity measurements. We have performed these reflectivity measurements from 100 to 20 000 cm^{-1} (0.01 to 2.48 eV) at room temperature using Fourier-transform infrared spectroscopy (FTIR) with the use of a Bruker 80v spectrometer, which is coupled to a Hyperion microscope. To obtain the absolute
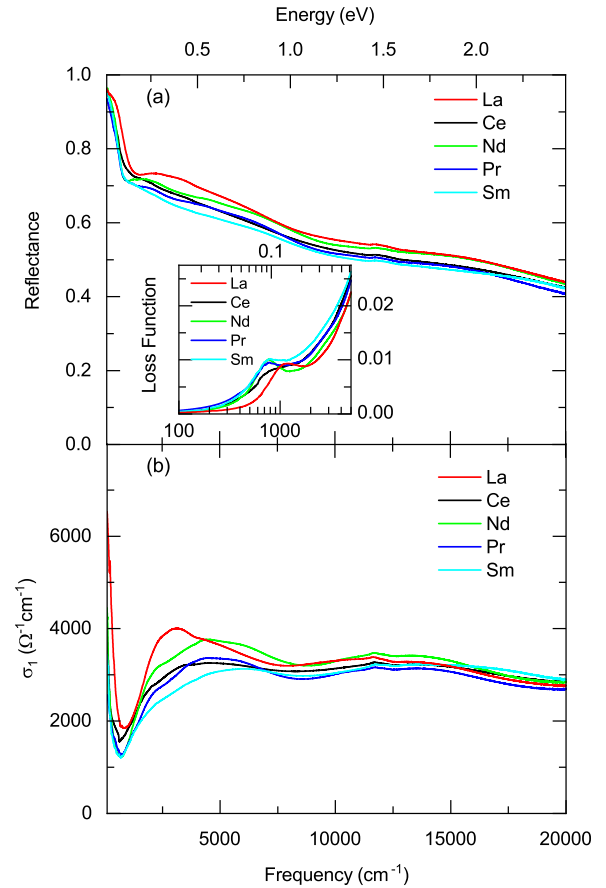

FIG. 1. (a) Room-temperature reflectance of five different compounds of the RAlSi family ($R = $ La, Ce, Nd, Pr, Sm) at room temperature. Inset: Loss function from 100 to 5000 cm^{-1} as an inset. (b) Corresponding optical conductivity σ_1 for all measured compounds.

reflectance of our samples, these have been aligned perpendicular to the incoming IR beam, which also holds for an aluminum mirror next to it serving as a reference. In the case of LaAlSi, additional low-temperature reflectivity measurements were carried out. By using resistivity values and volumetric data from the literature [7,8,15], these reflectance data were extrapolated in the low- and high-energy ranges, which is necessary to calculate the optical functions, such as the optical conductivity σ_1, the real part of the dielectric function ε_1, and the loss function $-\text{Im}(1/\varepsilon)$, from Kramers-Kronig relations using programs by David Tanner [22]. The optical functions have been analyzed with the REFFIT software [23] by fitting with the Drude-Lorentz model.

III. RESULTS AND DISCUSSION

The reflectance spectra displayed in Fig. 1(a) show a high value towards the low-energy range, indicating the metallic characteristics of the investigated materials of the RAlSi compound family. Also, a plasma edge is observed at around 900 cm^{-1} for all five compounds. For LaAlSi the plasma edge is located at the highest frequency, indicating that it has the strongest metallic character among the studied samples (see also the discussion of the plasmon peak position

below). Towards higher energy, the reflectance spectra show a very similar behavior for all compounds and are just varying slightly in their absolute value, therefore hinting at a similar electronic structure of the RAlSi materials in the higher energy regime. Especially noticeable is the merging of the reflectance spectra from approximately 16 000 to 20 000 cm^{-1}. Only the compound LaAlSi shows a broad bump at around 2500 cm^{-1}, and hence marks an exceptional behavior among the studied RAlSi materials.

The corresponding optical conductivity spectra σ_1 are depicted in Fig. 1(b). It is important to note that the optical conductivity spectra have a similar profile for all five compounds with only quantitative differences. This is in contrast to results reported for the closely related materials LaAlGe, CeAlGe, and PrAlGe, which exhibit different optical conductivity profiles already at room temperature [19,20]. Among the studied compounds, LaAlSi has the highest σ_1 value at the lowest studied wave number 100 cm^{-1}. NdAlSi exhibits the second highest value, and CeAlSi and SmAlSi do have very similar values at the low-frequency limit, although the value of CeAlSi is slightly higher, and PrAlSi has the lowest value. Besides the difference for the value of σ_1 at low energy (100 cm^{-1} or 0.01 eV) and the varying distinction of the first peak in the spectrum (2000 to 5500 cm^{-1}), the spectra of the five different compounds resemble a similar profile towards higher energy. This leads to the conclusion that the main differences in the materials lie in the low-energy regime, where the excitations of free charge carriers (Drude contribution) and the interband transitions between electronic bands in the direct vicinity of the Fermi energy contribute. The Lorentz contributions in the higher-energy range are very similar for all investigated materials and show no dependence on the rare-earth element R.

As the reflectance and optical conductivity data already suggest, the compound LaAlSi stands out in comparison to the other four studied compounds. This is also revealed by the position of the plasmon peak in the loss function (LF) [see the inset in Fig. 1(a)]. Although no absolute value can be obtained for the position of the plasmon peak, since the peak is not distinct enough, for the compounds of CeAlSi, NdAlSi, PrAlSi, and SmAlSi the plasmon peak is located at approximately the same frequency. However, for LaAlSi the peak position is obviously shifted to a higher value. The presence of a plasmon peak in the loss function also indicates the metallic character of all studied compounds.

In general, the position of the plasmon peak yields a value for the screened plasma frequency ω_{pl}^{scr}, which can serve as a measure for the metallic strength of a material. The value of ω_{pl}^{scr} can also be extracted from the zero crossing of the real part of the dielectric function ε_1 (see Fig. 2). The so-obtained ω_{pl}^{scr} values for all studied materials are depicted in the inset of Fig. 2. First, it can be seen that for low frequencies (< 1000 cm^{-1}), ε_1 takes large negative values, evidencing the metallic character of the investigated materials. Secondly, the negative values of ε_1 at high energies are caused by the rather pronounced interband transitions due to the presence of multiple energy bands in the vicinity of E_F. Thirdly, it is obvious that the screened plasma frequency is the highest for LaAlSi, since the zero crossing point is clearly set apart from the other four compounds towards higher energies. For the compounds
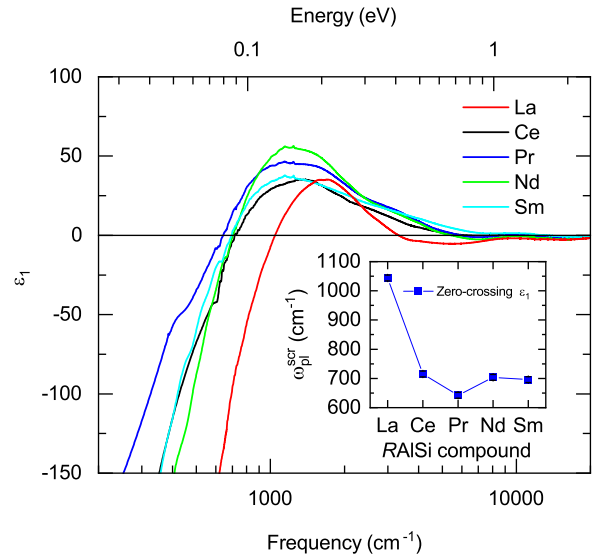

FIG. 2. Real part of the dielectric function ε_1 for all studied RAlSi compounds at room temperature. The inset shows the values of the screened plasma frequency ω_{pl}^{scr} determined by the zero-crossing of ε_1.

CeAlSi, PrAlSi, NdAlSi, and SmAlSi, the frequency of the zero crossing is roughly at the same position. The ω_{pl}^{scr} value for LaAlSi is approximately 1500 cm^{-1}, whereas for the compounds CeAlSi, NdAlSi, and SmAlSi, a value of around 700 cm^{-1} is obtained. The compound PrAlSi has the smallest value of 650 cm^{-1}. Most importantly, LaAlSi has by far the highest value of the screened plasma frequency, which is in accordance with the loss function, reflectance, and optical conductivity.

For quantitative analysis of the optical response functions, a Drude-Lorentz fitting model with one Drude component and six Lorentz oscillators was applied for all five RAlSi compounds. As an example, we show in Fig. 3 the fit of the optical conductivity σ_1 for PrAlSi together with the various fitting contributions. According to Hall resistivity measurements, the main charge-carrier type in the material LaAlSi are electrons [11], which justifies the implementation of only one Drude oscillator term in the fitting model. For other RAlSi compounds, the contribution of both electron and hole pockets to the transport, i.e., the multiband nature, has been pointed out. Nevertheless, we keep the same Drude-Lorentz fitting model (one Drude term only) for all studied materials for consistency reasons. We also point out that for none of the compounds was it necessary to include a second Drude term in the model in order to obtain a very good fit of both reflectivity and optical conductivity data simultaneously.

The optical conductivity spectrum has a similar profile for all five compounds, however there are quantitative differences: In LaAlSi the Lorentz oscillators L1 and L2 are shifted to lower energies as compared to the other compounds, implying slight differences in the electronic band structure close to E_F. The most pronounced differences are observed in the low-energy range, where the Drude term due to itinerant carrier excitations is located. The plasma frequency ω_{pl}, as obtained from the spectral weight of the Drude term, is
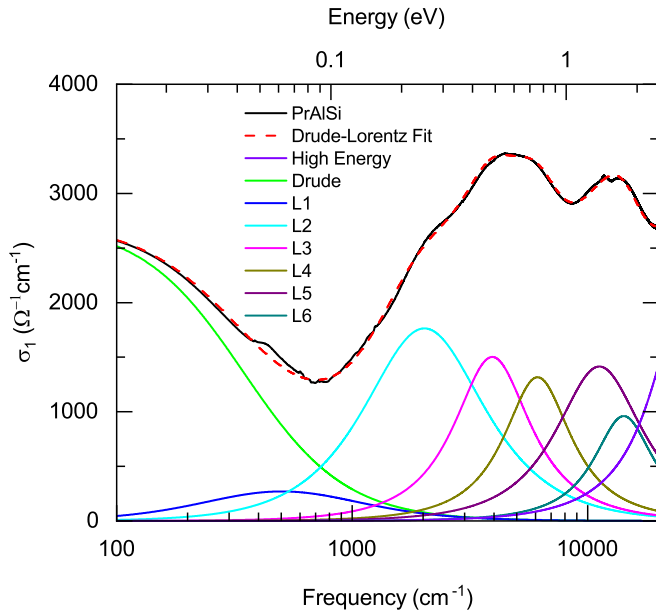
FIG. 3. Drude-Lorentz fit of the optical conductivity σ_1 of PrAlSi at room temperature. All Drude and Lorentz contributions in the measured range are plotted separately, while the "High-Energy" contribution represents the sum of all higher-energy Lorentz peaks.

FIG. 5. Interband optical conductivity of all studied RAlSi compounds at room temperature, as obtained by subtracting the Drude term from the total optical conductivity spectrum. The two regimes with the linear frequency dependences in $\sigma_{1,\text{interband}}$ are indicated by blue and orange areas, respectively. Please note that the marked areas only roughly highlight the two regimes, as there are quantitative differences among the studied materials regarding the limiting frequencies.

displayed in Fig. 4 as a function of a rare-earth element. In comparison, the compounds CeAlSi, PrAlSi, NdAlSi, and SmAlSi have a very similar value of the plasma frequency (~ 7500 cm^{-1}), and LaAlSi exhibits a much higher value ($\sim 12\,000$ cm^{-1}). It is important to note that the metallic characteristics of the studied RAlSi compounds, as evidenced by the pronounced Drude term, is rather surprising, since electronic band-structure calculations reveal an almost vanishing electronic density of states at the Fermi energy [24].

We furthermore note that the values of the screened plasma frequency calculated from the Drude spectral weight (taking into account the ϵ_1 value at around 1500 cm^{-1}) are slightly higher than the values as obtained from the zero crossing

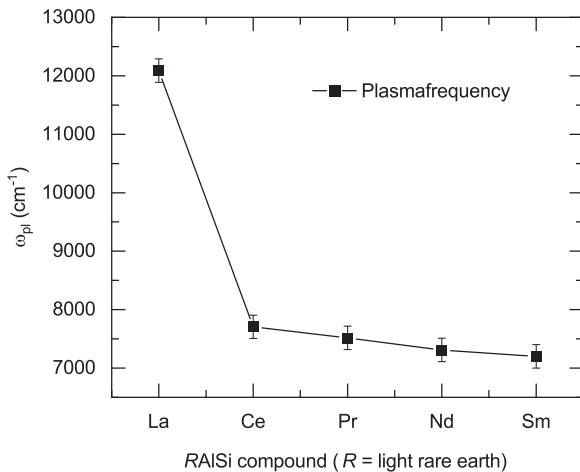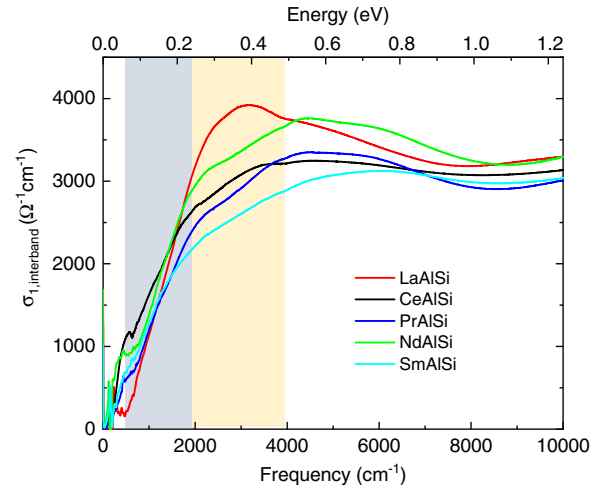of ϵ_1 (see the inset of Fig. 2). Such a discrepancy has been reported in the literature in several cases [25,26], and is due to the choice of the frequency for extracting the ϵ_1 value and the error bar of the optical parameters like the Drude spectral weight.

For all studied compounds, one notices that the optical conductivity σ_1 follows an ω-linear behavior above ~ 1000 cm^{-1}, i.e., in the frequency range of the interband excitations. For further analysis and interpretation of the interband transitions, we subtracted the Drude term from the total optical conductivity spectrum σ_1 and thus obtained the interband conductivity $\sigma_{1,\text{interband}}$, which is plotted in Fig. 5.

There are two linear regimes in $\sigma_{1,\text{interband}}$, as shown for PrAlSi and NdAlSi in Fig. 6 as examples. The steep linear increase in $\sigma_{1,\text{interband}}$ at low frequencies ($\omega > \Omega_1$) is followed by another linear frequency dependence for $\omega > \Omega_2$, however with a smaller slope, leading to a kink in the spectrum. This higher-energy linear frequency dependence (above Ω_2) extrapolates to a finite $\sigma_{1,\text{interband}}$ value in the $\omega \to 0$ limit. The two regimes with the linear frequency dependences in $\sigma_{1,\text{interband}}$ are indicated in Fig. 6 by blue and orange areas, respectively. For LaAlSi, the higher-energy regime is least developed among the studied materials.

A linear-in-frequency behavior of the interband optical response is a characteristic fingerprint for the existence of Dirac and Weyl fermions in condensed matter. Namely, the interband optical response of such linear Dirac/Weyl cones is predicted to follow a linear dependence in frequency ω for a three-dimensional (3D) system according to [27–30]

$$\sigma_1(\omega) = \frac{Ne^2}{24\pi\hbar v_F}\omega\Theta(\omega - 2E_F), \tag{1}$$

where N is the number of Weyl points (lifting the spin degeneracy) and v_F is the average Fermi velocity. A possible shift

FIG. 4. Plasma frequency ω_{pl} obtained from the spectral weight of the Drude term for all studied RAlSi compounds at room temperature.
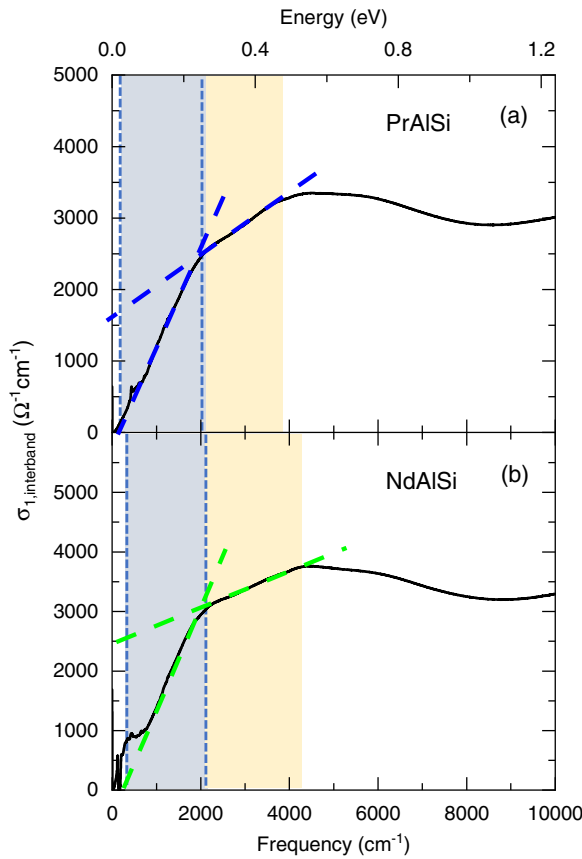
FIG. 6. Interband optical conductivity spectra of (a) PrAlSi and (b) NdAlSi from 0 to 10 000 cm^{-1} at room temperature. In both spectra, two linear fits are inserted (dashed lines), highlighting the characteristic features of type-II Weyl nodes. The two regimes with the linear frequency dependences in $\sigma_{1,\text{interband}}$ are indicated by blue and orange areas, respectively, and limited by vertical, dashed lines.

of the Dirac node away from the Fermi energy is taken into account by the Heaviside step function Θ, describing the Pauli blocking edge. For 3D Weyl semimetals, one or two quasi-linear regions with different slopes are predicted [5,27,28], as described in more detail below. The characteristic linear frequency dependence of the interband optical response was indeed observed in the 3D Dirac semimetal ZrTe$_5$ and in the 3D Weyl semimetal TaAs: While for ZrTe$_5$ a linear behavior in σ_1 was observed in the low-frequency range [31], for TaAs two ω-linear components with different slopes were found [32]. In TaAs, the two ω-linear components in the σ_1 spectrum are visible already at room temperature and persist down to low temperatures [33].

According to theoretical predictions [5], for a time-reversal symmetry breaking WSM the Weyl cones are shifted along the direction in k-space, whereas for a space-inversion breaking WSM the cones are shifted in energy but stay situated at the same position in k-space. The latter situation results in an optical conductivity spectrum, where two linear-in-frequency ranges with different slopes are formed. The first linear slope is caused by excitations within the same Dirac cone, which requires less energy for electronic interband excitations in comparison. When the energy is high enough, these

excitations can also be found between the two shifted Weyl cones. Thus, two linear ranges with different slopes are observed [5]. Accordingly, from the number of linear-in-frequency regimes in σ_1 one could in principle distinguish between time-reversal symmetry breaking and space-inversion breaking WSMs.

On the other hand, also a tilting of the Weyl cones in reciprocal space can cause two linear-in-frequency regimes in the optical conductivity spectrum. The difference between type-I and type-II WSMs was described by Carbotte [34] based on the degree of tilting of the Weyl cones, given by the tilting parameter $\hat{w}$. Without tilting, the value $\hat{w} = 0$ is assigned. For a small tilt, the values of $\hat{w}$ vary between 0 and 1. These states describe the case of a type-I WSM according to Ref. [34]. For a strong tilt, where the value of $\hat{w}$ exceeds 1, a type-II WSM is formed. The value $\hat{w} = 1$ describes the case for a tilt of $\pi/2$ into the plane perpendicular to the energy axis [34]. A type-II WSM is also referred to as an overtilted Weyl cone in energy-momentum space. Based on the optical conductivity, the two types of WSMs can be differentiated by looking at the linear ranges in the spectrum: For a type-I WSM, the linear-in-frequency behavior at frequencies $\omega > \Omega_2$ can be extrapolated to zero frequency, so that it crosses the origin. This is different for type-II WSM: These are also described by two linear slopes in the optical conductivity, where the extrapolation of the linear range at $\omega > \Omega_2$ yields an interception of the y-axis at a finite conductivity value. Furthermore, the slope of the higher-energy linear range ($\omega > \Omega_2$) is expected to decrease with an increasing tilt of the Weyl nodes [34]. Please note that Ref. [34] considers Weyl nodes shifted away from the Fermi energy (see below).

According to the optical data obtained in this study, two linear ranges with different slopes are found in the $\sigma_{1,\text{interband}}$ spectra of the studied RAlSi materials (see Fig. 6). Furthermore, the $\omega \to 0$ extrapolation of the linear slope in the higher-energy regime shows the crossing of the y-axis at a finite conductivity value, indicating that the investigated materials of the RAlSi compound family are in fact type-II WSMs formed by the space-inversion symmetry breaking. The data therefore suggest that the studied materials are type-II Weyl semimetals, with mainly overtilted $\hat{w} > 1$ Weyl nodes in the energy-momentum space (see also below). However, it is important to note that in the case of LaAlSi both type-I and type-II Weyl nodes have been found and reported at $\sim$0.1 eV above E_F and exactly at E_F, respectively [11]. Indeed, for LaAlSi the higher-energy linear-in-frequency regime in the σ_1 spectrum (see Fig. 1) is less developed, which suggests a significant contribution of type-I Weyl nodes to excitations in the optical response. We also note that in the closely related compounds NdAlSi, CeAlSi, and LaAlGe, 40 type-I and type-II Weyl nodes in the vicinity of the Fermi level have been theoretically predicted upon inclusion of spin-orbit coupling [7,12,17].

In a recent study, optical conductivity data of the related materials LaAlGe and CeAlGe revealed the typical optical signatures of type-II Weyl fermions, namely two linear frequency dependences in the interband optical conductivity [19]. Interestingly, for PrAlGe only a single linear frequency dependence in $\sigma_{1,\text{interband}}$ was observed [20], which is a typical signature for type-I Weyl semimetals, as discussed above.

TABLE I. Frequencies Ω_1 and Ω_2, chemical potential μ, tilting parameter $\hat{w}$ of the Weyl nodes, and average Fermi velocity v_F of RAlSi compounds at room temperature, and for LaAlSi at room temperature and 5 K.

Material	Ω_1 (cm^{-1})	Ω_2 (cm^{-1})	μ (cm^{-1})	$\hat{w}$	v_F (10^4 ms^{-1})
LaAlSi (295 K, 5 K)	412	2238	505	1.45	36
CeAlSi (295 K)	0	1957	0	1	61
PrAlSi (295 K)	148	1933	160	1.17	45
NdAlSi (295 K)	230	2072	259	1.45	46
SmAlSi (295 K)	69	1622	72	1.09	60

For all three materials (LaAlGe, CeAlGe, PrAlGe), these signatures appear at much lower energies as compared to RAlSi, hence being not well separated from the free charge-carrier excitations, and they were much less developed at room temperature. For CeAlGe and PrAlGe, the role of f-electrons has been pointed out, namely mediating electronic correlations (Kondo coupling between f-electrons and conduction bands), which cause a renormalization of the topological bands, with the reduction of the Fermi velocity and the increase in the effective mass of charge carriers at low temperature [19,20]. Therefore, CeAlGe and PrAlGe have been suggested as correlated Weyl-Kondo systems. In contrast, LaAlGe does not possess f electrons and therefore is expected to be noncorrelated [19].

Comparing the optical response of RAlSi and RAlGe materials, we note that *all* RAlSi compounds of the present study show a similar profile of the optical conductivity spectrum at room temperature, i.e., above the magnetic ordering, revealing the typical signatures of type-II Weyl fermion excitations. In particular, we cannot confirm a type-I Weyl fermion behavior for PrAlSi in contrast to PrAlGe. Like LaAlGe, LaAlSi is expected to be noncorrelated as there are no f electrons, consistent with the observed highest Drude spectral weight (squared unscreened plasma frequency) among the RAlSi compounds (see Fig. 4). Following the analysis of the interband optical conductivity spectra in Ref. [19], we can extract the tilting parameter $\hat{w}$ of the Weyl cones, the chemical potential μ, and the average Fermi velocity v_F. According to Ref. [34], the parameters μ and v_F can be obtained from the limiting frequencies Ω_1 and Ω_2 using the equations $\Omega_1 = 2\mu/(1 + \hat{w})$ and $\Omega_2 = 2\mu/(\hat{w} - 1)$. The so-obtained parameters for the studied RAlSi compounds at room temperature are listed in Table I. For all studied materials RAlSi the tilting parameter $\hat{w}$ is 1 or greater than 1, suggesting an overtilt of the Weyl cones. Furthermore, from the slope of the linear-in-frequency behavior of the interband optical conductivity at $\omega > \Omega_2$ (see Fig. 6), the Fermi velocity can be estimated according to [34]

$$\sigma_1(\omega) = \frac{Ne^2}{24\pi\hbar v_F} \frac{1 + 3\hat{w}^2}{4\hat{w}^3} \omega. \quad (2)$$

For all studied compounds we set $N = 40$ [7,12,17]. The so-obtained values of the Fermi velocity v_F are included in Table I. The values of v_F for all compounds lie in the range $(35–61) \times 10^4$ ms^{-1}, in reasonable agreement with results from Shubnikov–de Haas oscillation measurements on SmAlSi and LaAlSi at low temperature [11,15,35]. For LaAlSi without f electrons and hence no low-temperature magnetic ordering, we also extracted the low-temperature parameters from corresponding optical data and found them to be independent of temperature. Finally, it is important to note that the v_F values of RAlSi are a factor of ~10 higher than for LaAlGe and CeAlGe [19], suggesting that the RAlSi materials are less correlated than RAlGe.

IV. CONCLUSION

In conclusion, we studied the optical response of the noncentrosymmetric compounds RAlSi (R = La, Ce, Pr, Nd, Sm) at room temperature in order to investigate their electronic structure and electronic excitations in the paramagnetic phase, in particular regarding the dependence on the rare-earth element R. Over the whole studied frequency range, the reflectivity and optical conductivity spectra show only minor differences between the materials CeAlSi, PrAlSi, NdAlSi, and SmAlSi, which all exhibit magnetic order at low temperatures. The main differences can be found in the frequency range below 7500 cm^{-1}, where the free charge-carrier excitations and low-frequency interband transitions occur. Especially the nonmagnetic LaAlSi compound stands out, as it exhibits the strongest metallic character according to its (screened) plasma frequency. Thus, mostly the electronic band structure close to the Fermi level seems to be affected by the variation of the rare-earth element R. Furthermore, two quasilinear ranges with different slopes are observed in the low-frequency optical conductivity spectrum, which indicates the existence of Weyl nodes in the vicinity of E_F. From the analysis of the linear-in-frequency behavior of the optical conductivity, we can conclude that the Weyl cones are mainly of type-II and are overtilted.

[1] N. P. Armitage, E. J. Mele, and A. Vishwanath, Weyl and Dirac semimetals in three-dimensional solids, Rev. Mod. Phys. **90**, 015001 (2018).

[2] B. Yan and C. Felser, Topological materials: Weyl semimetals, Annu. Rev. Condens. Matter Phys. **8**, 337 (2017).

[3] B. Q. Lv, H. M. Weng, B. B. Fu, X. P. Wang, H. Miao, J. Ma, P. Richard, X. C. Huang, L. X. Zhao, G. F. Chen, Z. Fang, X. Dai, T. Qian, and H. Ding, Experimental discovery of Weyl semimetal TaAs, Phys. Rev. X **5**, 031013 (2015).

[4] J.-R. Soh, F. de Juan, M. G. Vergniory, N. B. M. Schröter, M. C. Rahn, D. Y. Yan, J. Jiang, M. Bristow, P. Reiss, J. N. Blandy, Y. F. Guo, Y. G. Shi, T. K. Kim, A. McCollam, S. H. Simon, Y. Chen, A. I. Coldea, and A. T. Boothroyd, Ideal Weyl semimetal induced by magnetic exchange, Phys. Rev. B **100**, 201102(R) (2019).

[5] C. J. Tabert, J. P. Carbotte, and E. J. Nicol, Optical and transport properties in three-dimensional Dirac and Weyl semimetals, Phys. Rev. B **93**, 085426 (2016).

[6] H.-Y. Yang, B. Singh, J. Gaudet, B. Lu, C.-Y. Huang, W.-C. Chiu, S.-M. Huang, B. Wang, F. Bahrami, B. Xu, J. Franklin, I. Sochnikov, D. E. Graf, G. Xu, Y. Zhao, C. M. Hoffman, H. Lin, D. H. Torchinsky, C. L. Broholm, A. Bansil *et al.*, Noncollinear ferromagnetic Weyl semimetal with anisotropic anomalous Hall effect, Phys. Rev. B **103**, 115143 (2021).

[7] J.-F. Wang, Q.-X. Dong, Z.-P. Guo, M. Lv, Y.-F. Huang, J.-S. Xiang, Z.-A. Ren, Z.-J. Wang, P.-J. Sun, G. Li, and G.-F. Chen, NdAlSi: A magnetic Weyl semimetal candidate with rich magnetic phases and atypical transport properties, Phys. Rev. B **105**, 144435 (2022).

[8] M. Lyu, J. Xiang, Z. Mi, H. Zhao, Z. Wang, E. Liu, G. Chen, Z. Ren, G. Li, and P. Sun, Nonsaturating magnetoresistance, anomalous Hall effect, and magnetic quantum oscillations in the ferromagnetic semimetal PrAlSi, Phys. Rev. B **102**, 085143 (2020).

[9] E. Cheng, L. Yan, X. Shi, R. Lou, A. Fedorov, M. Behnami, J. Yuan, Y. Xu, Y. Xu, W. Xia, N. Pavlovskii, D. Peets, W. Zhao, Y. Wan, Y. Guo, S. Li, W. Yang, and B. Büchner, Tunable positions of Weyl nodes via magnetism and pressure in the ferromagnetic Weyl semimetal CeAlSi, arXiv:2301.03800.

[10] L. Wu, S. Chi, H. Zuo, G. Xu, L. Zhao, Y. Luo, and Z. Zhu, Field-induced Lifshitz transition in the magnetic Weyl semimetal candidate PrAlSi, npj Quantum Mater. **8**, 4 (2023).

[11] H. Su, X. Shi, J. Yuan, Y. Wan, E. Cheng, C. Xi, L. Pi, X. Wang, Z. Zou, N. Yu, W. Zhao, S. Li, and Y. Guo, Multiple Weyl fermions in the noncentrosymmetric semimetal LaAlSi, Phys. Rev. B **103**, 165128 (2021).

[12] S.-Y. Xu, N. Alidoust, G. Chang, H. Lu, B. Singh, I. Belopolski, D. S. Sanchez, X. Zhang, G. Bian, H. Zheng, M.-A. Husanu, Y. Bian, S.-M. Huang, C.-H. Hsu, T.-R. Chang, H.-T. Jeng, A. Bansil, T. Neupert, V. N. Strocov, H. Lin *et al.*, Discovery of Lorentz-violating type II Weyl fermions in LaAlGe, Sci. Adv. **3**, e1603266 (2017).

[13] C. Dhital, R. L. Dally, R. Ruvalcaba, R. Gonzalez-Hernandez, J. Guerrero-Sanchez, H. B. Cao, Q. Zhang, W. Tian, Y. Wu, M. D. Frontzek, S. K. Karna, A. Meads, B. Wilson, R. Chapai, D. Graf, J. Bacsa, R. Jin, and J. F. DiTusa, Multi-k magnetic structure and large anomalous Hall effect in candidate magnetic Weyl semimetal NdAlGe, Phys. Rev. B **107**, 224414 (2023).

[14] T. Wang, Y. Guo, and C. Wang, Structure and magnetic properties of RAlSi (R = light rare earth), Chin. Phys. B **30**, 075102 (2021).

[15] W. Cao, Q. Wang, C. Pei, L. Gao, Y. Zhao, C. Li, N. Yu, J. Wang, Y. Chen, J. Li, and Y. Qi, Quantum oscillations in Non-centrosymmetric Weyl semimetal SmAlSi, Chin. Phys. Lett. **39**, 047501 (2022).

[16] J. Gaudet, H.-Y. Yang, S. Baidya, B. Lu, G. Xu, Y. Zhao, J.-A. Rodriguez-Rivera, C.-M. Hoffmann, D.-E. Graf, D.-H. Torchinsky, P. Nikolić, D. Vanderbilt, F. Tafti, and C.-L. Broholm, Weyl-mediated helical magnetism in NdAlSi, Nat. Mater. **20**, 1650 (2021).

[17] A. P. Sakhya, C.-Y. Huang, G. Dhakal, X.-J. Gao, S. Regmi, B. Wang, W. Wen, R.-H. He, X. Yao, R. Smith, M. Sprague, S. Gao, B. Singh, H. Lin, S.-Y. Xu, F. Tafti, A. Bansil, and M. Neupane, Observation of Fermi arcs and Weyl nodes in a noncentrosymmetric magnetic Weyl semimetal, Phys. Rev. Mater. **7**, L051202 (2023).

[18] R. Lou, A. Fedorov, L. Zhao, A. Yaresko, B. Büchner, and S. Borisenko, Signature of weakly coupled f electrons and conduction electrons in magnetic Weyl semimetal candidates PrAlSi and SmAlSi, Phys. Rev. B **107**, 035158 (2023).

[19] M. Corasaniti, R. Yang, Z. Hu, M. Abeykoon, C. Petrovic, and L. Degiorgi, Evidence for correlation effects in noncentrosymmetric type-ii Weyl semimetals, Phys. Rev. B **104**, L121112 (2021).

[20] R. Yang, M. Corasaniti, C. C. Le, Z. Hu, J. P. Hu, C. Petrovic, and L. Degiorgi, Charge dynamics of a noncentrosymmetric magnetic Weyl semimetal, npj Quantum Mater. **7**, 101 (2022).

[21] W. Cao, N. Zhao, C. Pei, Q. Wang, Q. Zhang, T. Ying, Y. Zhao, L. Gao, C. Li, N. Yu, L. Gu, Y. Chen, K. Liu, and Y. Qi, Pressure-induced superconductivity in the noncentrosymmetric Weyl semimetals LaAlX (X = Si, Ge), Phys. Rev. B **105**, 174502 (2022).

[22] D. B. Tanner, Use of x-ray scattering functions in Kramers-Kronig analysis of reflectance, Phys. Rev. B **91**, 035123 (2015).

[23] A. B. Kuzmenko, Kramers-Kronig constrained variational analysis of optical spectra, Rev. Sci. Instrum. **76**, 083108 (2005).

[24] M. M. Piva, J. C. Souza, V. Brousseau-Couture, S. Sorn, K. R. Pakuszewski, J. K. John, C. Adriano, M. Côté, P. G. Pagliuso, A. Paramekanti, and M. Nicklas, Topological features in the ferromagnetic Weyl semimetal CeAlSi: Role of domain walls, Phys. Rev. Res. **5**, 013068 (2023).

[25] G. Li, W. Z. Hu, J. Dong, D. Qian, D. Hsieh, M. Z. Hasan, E. Morosan, R. J. Cava, and N. L. Wang, Anomalous metallic state of $Cu_{0.07}TiSe_2$: An optical spectroscopy study, Phys. Rev. Lett. **99**, 167002 (2007).

[26] G. Li, W. Z. Hu, D. Qian, D. Hsieh, M. Z. Hasan, E. Morosan, R. J. Cava, and N. L. Wang, Semimetal-to-semimetal charge density wave transition in $1T-TiSe_2$, Phys. Rev. Lett. **99**, 027404 (2007).

[27] C. J. Tabert and J. P. Carbotte, Optical conductivity of Weyl semimetals and signatures of the gapped semimetal phase transition, Phys. Rev. B **93**, 085442 (2016).

[28] P. E. C. Ashby and J. P. Carbotte, Chiral anomaly and optical absorption in Weyl semimetals, Phys. Rev. B **89**, 245121 (2014).

[29] P. Hosur, S. A. Parameswaran, and A. Vishwanath, Charge transport in Weyl semimetals, Phys. Rev. Lett. **108**, 046602 (2012).

[30] T. Timusk, J. P. Carbotte, C. C. Homes, D. N. Basov, and S. G. Sharapov, Three-dimensional Dirac fermions in quasicrystals as seen via optical conductivity, Phys. Rev. B **87**, 235121 (2013).

[31] R. Y. Chen, S. J. Zhang, J. A. Schneeloch, C. Zhang, Q. Li, G. D. Gu, and N. L. Wang, Optical spectroscopy study of the three-dimensional Dirac semimetal $ZrTe_5$, Phys. Rev. B **92**, 075107 (2015).

[32] B. Xu, Y. M. Dai, L. X. Zhao, K. Wang, R. Yang, W. Zhang, J. Y. Liu, H. Xiao, G. F. Chen, A. J. Taylor, D. A. Yarotski, R. P. Prasankumar, and X. G. Qiu, Optical spectroscopy of the Weyl semimetal TaAs, Phys. Rev. B **93**, 121110(R) (2016).

[33] S.-I. Kimura, H. Yokoyama, H. Watanabe, J. Sichelschmidt, V. Süß, M. Schmidt, and C. Felser, Optical signature of Weyl electronic structures in tantalum pnictides TaPn (Pn = P, As), Phys. Rev. B **96**, 075119 (2017).

[34] J. P. Carbotte, Dirac cone tilt on interband optical background of type-I and type-II Weyl semimetals, Phys. Rev. B **94**, 165111 (2016).

[35] L. Xu, H. Niu, Y. Bai, H. Zhu, S. Yuan, X. He, Y. Han, L. Zhao, Y. Yang, Z. Xia, Q. Liang, and Z. Tian, Shubnikov–de Haas oscillations and nontrivial topological states in Weyl semimetal candidate SmAlSi, J. Phys.: Condens. Matter **34**, 485701 (2022).